Journal of Power Sources 241 (2013) 509–516

Contents lists available at SciVerse ScienceDirect

Journal of Power Sources

journal homepage: www.elsevier.com/locate/jpowsour

Phase structures and electrochemical properties of $La_{0.8-x}Gd_{0.2}Mg_xNi_{3.1}Co_{0.3}Al_{0.1}$ hydrogen storage alloys

Zhijie Gao [a], Yongchun Luo [a,b,*], Rongfeng Li [a], Zhen Lin [a], Long Kang [a]

[a] Department of Materials Science and Engineering, Lanzhou University of Technology, Lanzhou 730050, PR China
[b] State Key Laboratory of Advanced Non-Ferrous Materials, Lanzhou University of Technology, Lanzhou 730050, PR China

HIGHLIGHTS

- The substitution of Gd for La in the A_2B_7-type electrode alloy was scarcely any reported before.
- The seal-annealed alloys can control loss of Mg elements during preparation.
- The lower Mg content was adopted in order to improve the cycle stability of the alloy.
- The relationship between the electrochemical performance and the Mg content was provided.

ARTICLE INFO

Article history:
Received 27 August 2012
Received in revised form
30 November 2012
Accepted 15 January 2013
Available online 11 May 2013

Keywords:
Hydrogen storage alloy
Magnesium
Alloy phase structure
Hydrogen absorption property
Electrochemical properties

ABSTRACT

$La_{0.8-x}Gd_{0.2}Mg_xNi_{3.1}Co_{0.3}Al_{0.1}$ ($x = 0.1–0.5$) hydrogen storage alloys are prepared by an induction melting followed by annealing treatment for 168 h at 1173 K in a sealed stainless steel tube. Instrumentation analyses indicate that the chemical composition and crystalline phase structure of these annealed alloys closely depended on the Mg content (x). At lower x than 0.25, the main phase is the Ce_2Ni_7-type phase and its phase abundance is 93.4 wt.%. When $x > 0.2$, the alloys are composed three phases, A_2B_7-type, $CaCu_5$-type and $PuNi_3$-type structure, in which phase abundance of the $PuNi_3$- and $CaCu_5$-type phase increases to 44.99 wt.% and 44.8 wt.% respectively. When Mg is controlled at $x < 0.3$, the volume of unit cell of Ce_2Ni_7-type decreases from 0.5391 nm^3 to 0.5170 nm^3. Hydrogen absorption capacity reaches maximum value (1.43 wt.%) at Mg = 0.15, whereas the absorption of hydrogen storage content decreases with the x increase, accordingly. Electrochemical measurements indicates $La_{0.65}Gd_{0.2}Mg_{0.15}Ni_{3.1}Co_{0.3}Al_{0.1}$ alloy electrode exhibits the maximum electrochemical discharge capacity of 391.4 mAh g^{-1} and the best cyclic stability S_{100} of 92.0%.

1. Introduction

La–Mg–Ni intermetallic alloys are promising electrode materials for the advanced Ni-metal hydride batteries. Their electrochemical discharge capacity reaches 410 mAh g^{-1}, 30% superior to that of the $LaNi_5$-based electrodes [1]. Rare-earth-based AB_5-type alloy and Zr-based Laves phase alloy have been commercialized successfully as Ni/MH secondary cell negative materials [2,3], but low capacity of AB_5-type alloy electrodes and difficult activation characteristics of Laves phase alloy electrodes limit the extensive application [4,5]. Recently, R–Mg–Ni-based (R = rare earths, Y, Ca) alloys are considered as promising negative electrode materials due to their higher capacity than commercial AB_5-type alloys [6].

R–Mg–Ni-based alloys relevant for electrochemical applications are related to the binary La–Ni intermetallic compounds of $PuNi_3$- and Ce_2Ni_7-types of crystalline structures. $LaMg_2Ni_9$ intermetallic crystallizing in the trigonal $PuNi_3$-type structure was first reported by Kadir et al. [7,8]. Its crystal structure is a stacking of the $LaNi_5$ (Haucke $CaCu_5$ type) and $MgNi_2$ (Laves $MgZn_2$ type) slabs along the trigonal [001] axis. Initial study of hydrogen absorption–desorption properties of $LaMg_2Ni_9$ [7] show its rather small hydrogen storage capacity of ~0.3 wt.%. This low value was explained by an inertness of the $MgNi_2$ slab to hydrogen absorption, similar to the properties of the individual $MgNi_2$ Laves type compound, which does not absorb hydrogen at conventional hydrogenation conditions [8].

Later research, however, showed that A_2B_7-type alloy of La–Mg–Ni system, which is Ce_2Ni_7-type superlattice structure, had

* Corresponding author. State Key Laboratory of Advanced Non-Ferrous Materials, Lanzhou University of Technology, Lanzhou 730050, PR China. Tel.: +86 931 297 4813; fax: +86 931 280 6962.
E-mail addresses: gaozhijie1983@126.com (Z. Gao), luoyc@lut.cn (Y. Luo).

0378-7753/$ – see front matter © 2013 Elsevier B.V. All rights reserved.
http://dx.doi.org/10.1016/j.jpowsour.2013.01.199

relatively good electrochemical properties [9–13]. Zhang et al. [12] found that the Ce_2Ni_7-type alloys of the ternary $La_{2-x}Mg_xNi_{7.0}$ were dominated in the x range $0.3 < x < 0.5$, with the unit cell volumes linearly decreasing with the La/Mg ratio increase. In parallel, it is observed an increase in the stability of the hydrides and an enhancement of the electrochemical discharge capacities, reaching 389 mAh g^{-1} in maximum for the composition $La_{1.5}Mg_{0.5}Ni_7$. However, cyclic stability of the alloy needs to be improved. Yasuoka et al. [13] reported that the cyclic stability of the Ce_2Ni_7-type electrode alloy $Mm_{0.83}Mg_{0.17}Ni_{3.1}Al_{0.2}$ is better than the commercial AB_5-type alloy, but a low capacity of 340 mAh g^{-1}.

Recent study of the phase diagram of the La–Mg–Ni system [14–16] showed that magnesium dramatically affects the hydrogenation–dehydrogenation behaviors and electrochemical properties of the ternary La–Mg–Ni-based $PuNi_3$- and Ce_2Ni_7-type alloys, allowing a fine tuning of the stabilities of the formed hydrides and optimization of their behaviors relevant for different applications. We have also obtained alloys with higher capacity retention rate by partial replacement of La by Gd. The solubility data of Gd in alkaline electrolyte is minimum, what is more, Rietveld analysis fitting as well as EPMA and WDS indicates that the electrochemical cyclic stability is obviously improved under low-Mg and B-site multi-component design by increasing the phase abundance of Ce_2Ni_7-type [17].

The overarching goal of this research is to improve the hydrogen storage capacity and cyclic stability of $La_{0.8-x}Gd_{0.2}Mg_xNi_{3.1}Co_{0.3}Al_{0.1}$ intermetallics. It is also aimed to understand the dependence of the Mg content on the crystalline structures and performance of the above intermetallics. The contribution of this study lies in achievement of improved cyclic stability ($S_{100} = 92\%$) while the discharge capacity was maintained at 391.4 mAh g^{-1}. More contribution is needed to know about the influence of the Mg/RE substitution ratio on the structural and electrochemical properties.

2. Experiment

2.1. Materials

Hydrogen storage alloys with various formulations ($La_{0.8-x}Gd_{0.2}Mg_xNi_{3.1}Co_{0.3}Al_{0.1}$ $x = 0.1$–0.5) were prepared by induction melting approach at 0.4 MPa of Ar atmosphere. The ingots were wrapped in a thallium (Ta) foil, sealed in stainless steel tubes under Ar pressure (0.1 MPa) and annealed for 168 h at 1173 K. Due to the high vapor pressure of Mg and rare earth elements, 10 wt.% excess Mg, 5 wt.% excess La and 5 wt.% excess Gd element was necessary during melting. The purity of all elements was above 99 wt.%.

2.2. Characterization

The annealed alloys were ground mechanically into powders (<38 μm) for X-ray diffraction (XRD) measurements. The powders ranged from 54 μm to 61 μm were used as electrode for electrochemical test. XRD measurements were performed on a Rigaku D/max-2400 diffractometer with Cu radiation and a power of 40 kV × 150 mA. The XRD pattern was recorded in the range from 15° to 90° with scanning rate of 4° min^{-1}. Then the collected data were analyzed by the Rietveld method using Fullprof 2K software [18,19] to get the lattice parameters and phase abundance.

The microscopic structure and the composition for annealed alloys were examined by scanning electron microscope (SEM) equipped with energy dispersive spectroscopy (EDS) on a JSM-5000LV instrument (JEOL). The voltage was controlled at 5 or 15 kV and beam current at 100 nA. The chamber pressure and field emission gun pressure were controlled at 3.5×10^{-5} Torr and 3.0×10^{-9} Torr for high resolution.

The Mg content in alloys was determined by the inductively coupled plasma (ICP) method. Pressure composition isotherm (PCT) tests were measured using a Sieverts-type apparatus (Beijing Nonferrous Metal Research Institute, China) at 298 K. Prior to formal measurements, powder samples were evacuated at 373 K and 1×10^{-4} Pa for at least 2 h in resistance furnace to remove the impurities. Then, the alloys were hydrided under a hydrogen pressure of ~4.5 MPa and dehydrided to ~0.0005 MPa to measure the hydriding–dehydriding at 333 K for three times.

2.3. Electrochemical measurement

Alloy electrodes were prepared by cold pressing the mixture of alloy power and carbonyl nickel power at the weight ratio of 1:3 under 20 MPa pressure to form a pellet of 10 mm in diameter. Electrochemical measurements were performed at 293 K in a standard open tri-electrode electrolysis cell consisting of alloy electrode, a sintered $Ni(OH)_2$/NiOOH anode and a Hg/HgO reference electrode immersed in 6 M KOH electrolyte. Each electrode was discharged to cut-off potential −0.6 V vs. Hg/HgO reference electrode. Electrodes were charged/discharged at 60 mA g^{-1} when activated; Electrodes were charged/discharged at 300 mA g^{-1} when examined for cyclic stability. The high rate dischargeability (HRD) was determined by examining the discharge capacity at various discharge current density and defined as the following equation:

$$\mathrm{HRD} = \frac{C_d}{C_d + C_{60}} \times 100\% \quad (1)$$

where C_d is the discharge capacity at I_d current density, C_{60} is the residual discharge capacity at I_{60} current density after an alloy electrode is discharged at I_d current density.

To investigate the electrocatalytic activity and kinetics character of alloy electrodes, linear polarization, anodic polarization and hydrogen diffusion in alloy bulk were performed on CHI660a electrochemical work station after alloy electrodes were activated.

Table 1
Chemical composition analyses of La–Mg–Ni alloys by ICP.

Samples	Element content (wt.%)						Chemical composition	B/A
	La	Gd	Mg	Ni	Co	Al		
$x = 0$	32.03	9.21	0	52.81	5.14	0.81	$La_{0.80}Gd_{0.20}Ni_{3.11}Co_{0.30}Al_{0.10}$	3.51
$x = 0.10$	29.06	9.50	0.68	54.71	5.25	0.80	$La_{0.70}Gd_{0.20}Mg_{0.10}Ni_{3.13}Co_{0.30}Al_{0.10}$	3.53
$x = 0.15$	27.94	9.46	1.03	55.44	5.33	0.79	$La_{0.66}Gd_{0.20}Mg_{0.14}Ni_{3.11}Co_{0.30}Al_{0.10}$	3.51
$x = 0.20$	25.79	9.95	1.41	56.91	5.54	0.84	$La_{0.60}Gd_{0.21}Mg_{0.19}Ni_{3.16}Co_{0.31}Al_{0.10}$	3.57
$x = 0.25$	24.27	9.76	1.80	57.81	5.59	0.82	$La_{0.56}Gd_{0.20}Mg_{0.24}Ni_{3.17}Co_{0.31}Al_{0.10}$	3.58
$x = 0.30$	22.83	9.23	2.39	58.91	5.71	0.93	$La_{0.51}Gd_{0.18}Mg_{0.31}Ni_{3.12}Co_{0.30}Al_{0.11}$	3.53
$x = 0.40$	18.72	10.45	3.29	60.64	5.91	0.98	$La_{0.40}Gd_{0.20}Mg_{0.40}Ni_{3.07}Co_{0.30}Al_{0.11}$	3.48
$x = 0.50$	14.58	10.59	4.37	63.28	6.16	1.02	$La_{0.30}Gd_{0.19}Mg_{0.51}Ni_{3.06}Co_{0.30}Al_{0.11}$	3.47

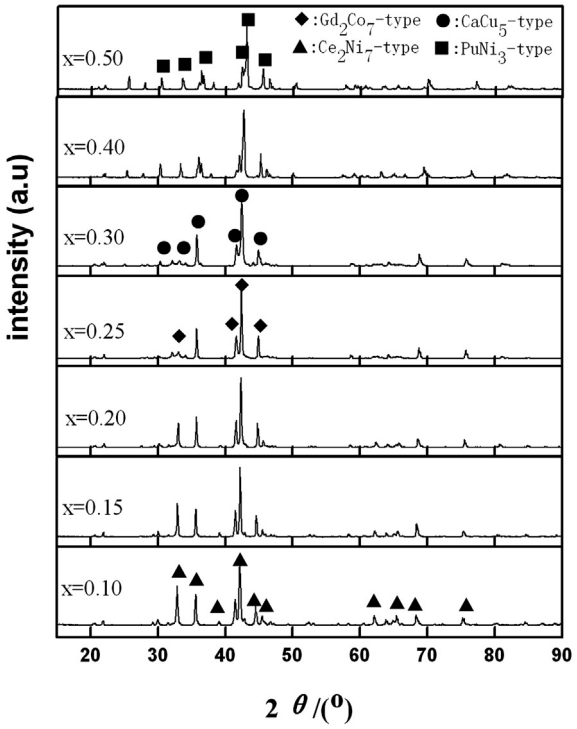

Fig. 1. XRD patterns for $La_{0.8-x}Gd_{0.2}Mg_xNi_{3.1}Co_{0.3}Al_{0.1}$ ($x = 0.1$–0.5) annealed alloys.

The linear polarization, and anodic polarization, and Tafel polarization curves were measured by scanning the electrode potential at a rate of 0.1 mV s^{-1} from −5 to 5 mV (vs. open circuit potential) and 5 mV s^{-1} from open circuit potential to −0.45 V (vs. Hg/HgO reference electrode) and 1 mV s^{-1} from −1.1 to −0.3 V (vs. Hg/HgO reference electrode) at 50% depth of discharge (DOD), respectively.

3. Result and discussion

3.1. Chemical composition of the alloy and identification of phases by X-ray diffraction

Table 1 lists the chemical compositions of the alloys measured after annealing treatment. It was confirmed that loss of Mg and rare earth elements during preparation was negligible. Fig. 1 shows the

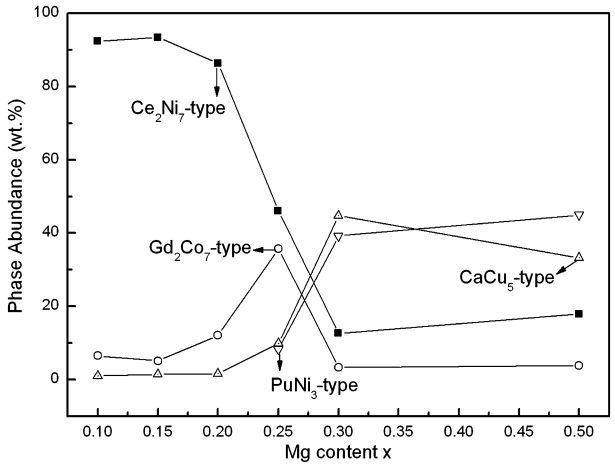

Fig. 3. Phase abundance variation curves for different annealed alloys.

XRD patterns for rare earth–Mg–Ni-based alloys with different Mg content and Figs. 2 and 3 shows the Rietveld refinement patterns of $La_{0.8-x}Gd_{0.2}Mg_xNi_{3.1}Co_{0.3}Al_{0.1}$ ($x = 0.15$, 0.25) alloys at 1173 K annealing treatment and the evolution of phase abundance vs. the annealing alloys, respectively. Structure characteristics of different annealed alloys are tabulated in Table 2 and the back scattering electron images of the alloys are pictured in Fig. 4. The main phase for $x = 0.1$–0.2 can be identified as Ce_2Ni_7-type phase just as shown in Fig. 4 (No. 1 ~ 3). Ce_2Ni_7-type phase became main phase (>86 wt.%) for $x \leq 0.2$ and then an impurity phase when $x \geq 0.25$. On the other hand, the abundance of $(La,Mg)(Ni,Co)_3$ phase increased from 8.25 wt.% ($x = 0.25$) to 44.99 wt.% ($x = 0.5$) and that of $LaNi_5$ phase increased from 1.06 wt.% ($x = 0.1$) to 44.8 wt.% ($x = 0.3$) then decreased to 33.3 wt.% ($x = 0.5$). At the same time, abundance of Gd_2Co_7-type phase also dramatically increased with rise of Mg content ($x = 0.1$–0.25). These experiment results show that Mg content for $x = 0.1$–0.2 benefited the formation of Ce_2Ni_7-type phase best. When $x > 0.2$, the composition of alloys was not very homogeneous just as shown in Fig. 4 (No. 4 ~ 6) in which there are some $La(Ni,Co)_5$ phase, $(La,Mg)_2(Ni,Co)_7$ phase, and $(La,Mg)(Ni,Co)_3$ phase. Presence of $(La,Mg)(Ni,Co)_3$ phase and increasing of $La(Ni,Co)_5$ phase indicate that Ce_2Ni_7-type crystal structure may disintegrate as Mg content increases, which are attributed to $2A_2B_7 = 3AB_3 + AB_5$. $(La,Mg)(Ni,Co)_3$ phase can hold more Mg content.

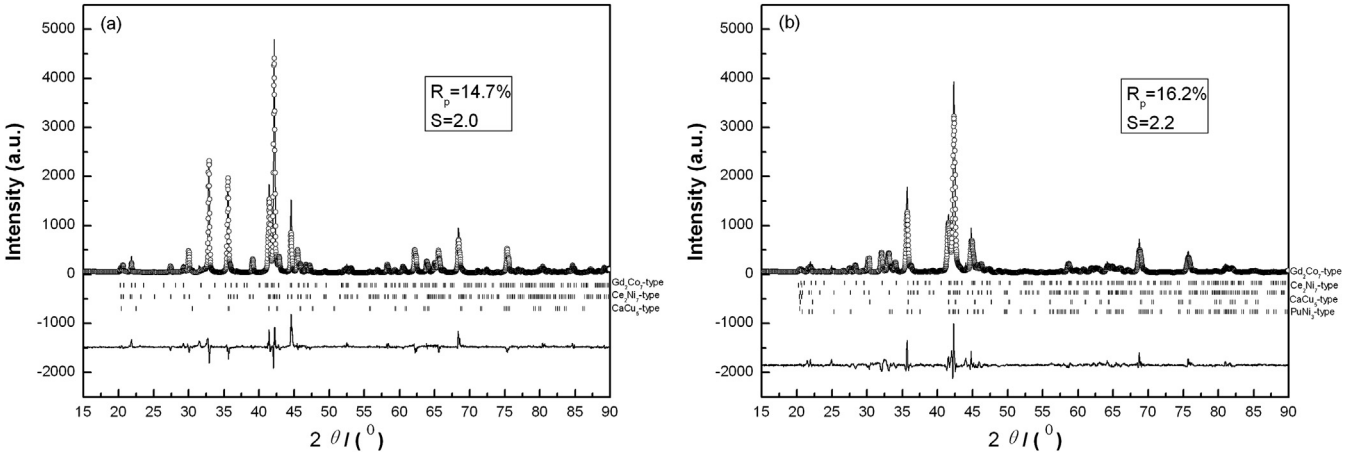

Fig. 2. Rietveld refinement patterns at $x = 0.15$, 0.25 for $La_{0.8-x}Gd_{0.2}Mg_xNi_{3.1}Co_{0.3}Al_{0.1}$ alloy: (a) $x = 0.15$ (b) $x = 0.25$.

Table 2
Characteristics of phases for different annealed alloys.

Alloys (x)	Phase	Lattice constants				Phase abundance (wt.%)	EDS analysis
		a/nm	c/nm	V/nm^3	c/a		
$x = 0.1$	Ce_2Ni_7-type	0.5047	2.4441	0.5391	4.843	92.4	–
	Gd_2Co_7-type	0.5003	3.6637	0.7942	7.323	6.53	–
	$CaCu_5$-type	0.5036	0.3992	0.0877	0.793	1.06	–
$x = 0.15$	Ce_2Ni_7-type	0.5041	2.4378	0.5366	4.836	93.4	$La_{0.617}Gd_{0.21}Mg_{0.173}Ni_{3.09}Co_{0.31}Al_{0.08}$
	Gd_2Co_7-type	0.5104	3.6650	0.8267	7.181	5.13	
	$CaCu_5$-type	0.5037	0.3956	0.0870	0.785	1.47	$La_{0.74}Gd_{0.18}Mg_{0.08}Ni_{4.39}Co_{0.3}Al_{0.15}$
$x = 0.2$	Ce_2Ni_7-type	0.5032	2.4291	0.5326	4.827	86.38	–
	Gd_2Co_7-type	0.4978	3.6118	0.7752	7.256	12.04	–
	$CaCu_5$-type	0.5032	0.3912	0.0858	0.777	1.59	–
$x = 0.25$	Ce_2Ni_7-type	0.5016	2.4191	0.5271	4.823	46.08	
	Gd_2Co_7-type	0.5019	3.6310	0.7922	7.235	35.71	
	$CaCu_5$-type	0.5016	0.4003	0.0872	0.798	9.96	
	$PuNi_3$-type	0.5027	2.4056	0.5266	4.785	8.25	
$x = 0.3$	Ce_2Ni_7-type	0.4988	2.3994	0.5170	4.810	12.63	–
	Gd_2Co_7-type	0.5008	3.5991	0.7817	7.187	3.35	–
	$CaCu_5$-type	0.4997	0.4002	0.0865	0.801	44.8	$La_{0.5}Gd_{0.20}Mg_{0.12}Ni_{3.14}Co_{0.33}Al_{0.06}$
	$PuNi_3$-type	0.4971	2.4017	0.5140	4.831	39.21	$La_{0.45}Gd_{0.20}Mg_{0.31}Ni_{2.73}Co_{0.32}Al_{0.04}$
$x = 0.5$	Ce_2Ni_7-type	0.4905	2.4166	0.5035	4.927	17.94	–
	Gd_2Co_7-type	0.4974	3.6524	0.7826	7.343	3.77	–
	$CaCu_5$-type	0.4981	0.3999	0.0859	0.803	33.3	–
	$PuNi_3$-type	0.4937	2.3887	0.5041	4.838	44.99	–

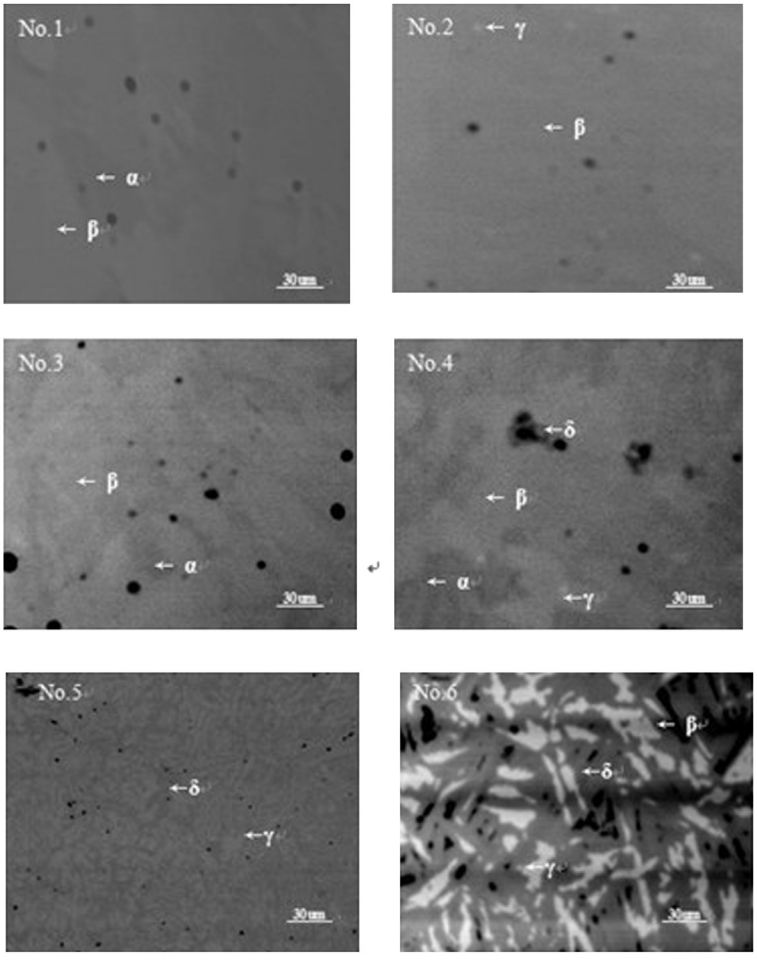

(No.1) x=0.1; (No.2) x=0.15; (No.3) x=0.2; (No.4) x=0.25; (No.5) x=0.3; (No.6) x=0.5

(α: Gd_2Co_7 type, β: Ce_2Ni_7 type, γ: $CaCu_5$ type, δ: $PuNi_3$ type)

Fig. 4. Back scattered electron images for different alloys.

Table 2 also tabulates the lattice parameters of alloys and Fig. 5 illustrates the Ce_2Ni_7-type lattice parameters as a function of Mg content (x), it can be seen that the increase of Mg content in alloys leads to the decrease of lattice parameters with a linear relationship, among which the cell volume decreases from 0.5391 nm^3 ($x = 0.1$) to 0.517 nm^3 ($x = 0.3$) which should be attributed to the difference of atomic radius between Mg (160 pm) and rare earth (La: 187.7 pm, Gd: 180.2 pm). Besides, the ratio of c/a also decreases with the increase of Mg content, it indicates that the change of the Ce_2Ni_7-type unit cell is anisotropic, and anisotropic change of Ce_2Ni_7-type unit cell is different obviously from isotropic change of $PuNi_3$-type unit cell [20]. However, because of the smaller atomic radius of Mg, Gd_2Co_7-type phase increases with rise of Mg content [21].

3.2. Hydrogen absorption P–C isotherm

Fig. 6 shows the hydrogen absorption P–C isotherm at 298 K. It is noted that the slope of hydrogen–absorption curve is large of $x = 0.1$, and it is obvious from Fig. 7 that the amorphous tendency becomes obvious, which may be due to the effect of Mg content. Although the phase abundance of Ce_2Ni_7-type is 92.4 wt.% at $x = 0.1$, the stoichiometric ratio of Mg element is only 0.1, the reversible storage capacity became bad. As the Mg content increases, the hydrogen storage capacity and the hydrogen absorption plateau become distinct, the characteristics of hydrogen absorption are listed in Table 3. It can be seen that the hydrogen storage capacity increases firstly 0.97 wt.% ($x = 0.1$) to 1.43 wt.% ($x = 0.15$) and then decreases to 0.23 wt.% ($x = 0.5$) and. With the increase of Mg content, the plateau pressure of hydrogen absorption rises gradually from 0.1 atm to 7.32 atm ($x = 0.4$). This indicates that it could be related with the content of Mg element and main phase abundance of each alloys, which can improve the amorphous tendency and hydrogen absorption capacity after hydrogenation, respectively.

So, when $x = 0.15$–0.2, the phase abundance of Ce_2Ni_7-type was ~90 wt.%, the addition of Mg element can improve reversible ability of hydrogen absorption process for Ce_2Ni_7-type alloys and hydrogen storage capacity of Ce_2Ni_7-type phase is bigger [12], so the absorption plateau became flatter and wider. When $x = 0.25$–0.5, with the increase of $CaCu_5$- and $PuNi_3$-type phase, the absorption plateau became higher and narrower. Two absorption plateaus appear for $x = 0.4$. It is noted that the isotherms are composed of two parts (a and b), the part (b) may be originated from $LaNi_5$ phase which has obvious plateau of pressure in a range from 1 atm to 10 atm [22], then the part (a) is originated from $PuNi_3$-type phase really. Finally, it indicates that the addition of Mg element can improve reversible ability of hydrogen absorption process for Ce_2Ni_7-type alloys.

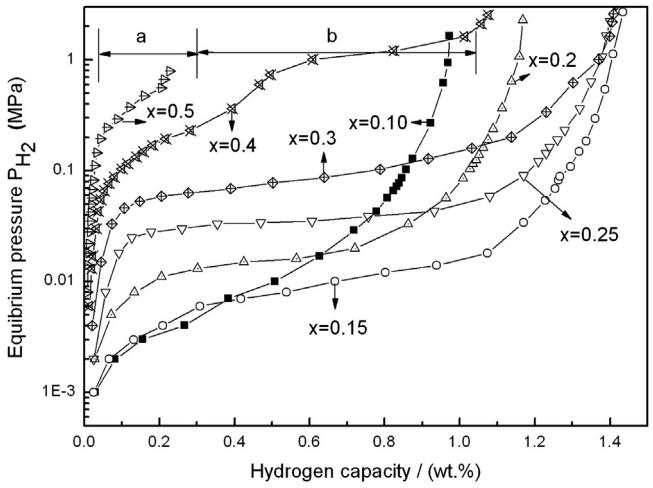

Fig. 6. P–C isotherms of for $La_{0.8-x}Gd_{0.2}Mg_xNi_{3.1}Co_{0.3}Al_{0.1}$ ($x = 0.1$–0.5) annealed alloys at 298 K.

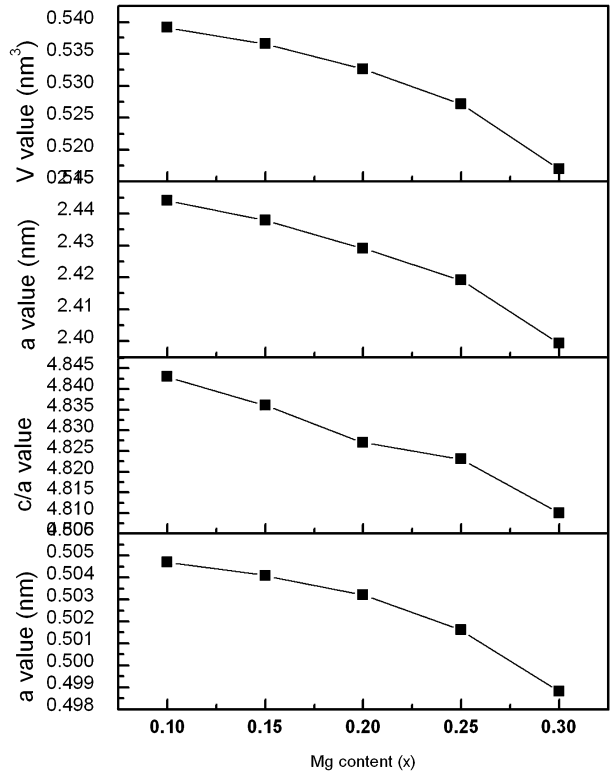

Fig. 5. Lattice parameters of Ce_2Ni_7 type phase as a function of Mg content (x) for $La_{0.8-x}Gd_{0.2}Mg_xNi_{3.1}Co_{0.3}Al_{0.1}$ ($x = 0.1$–0.3) annealed alloys.

3.3. Charge/discharge characteristics

Fig. 8 shows the activation curves of different alloy electrodes, and Table 4 summarizes electrochemical performance of different alloy electrodes. It can be found that all of alloy electrodes exhibited

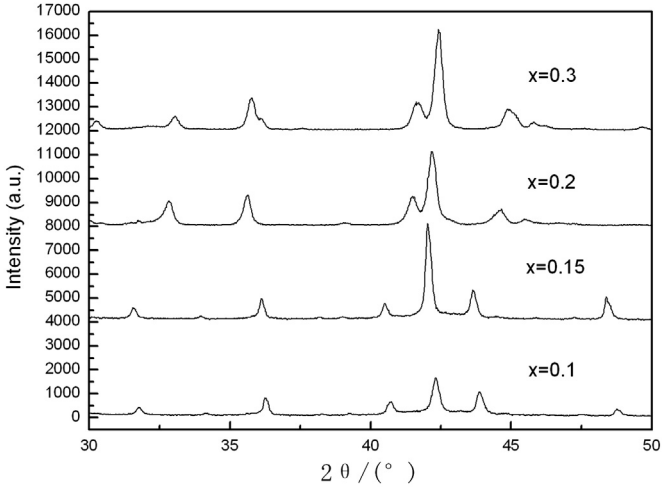

Fig. 7. XRD patterns of hydrides of $La_{0.8-x}Gd_{0.2}Mg_xNi_{3.1}Co_{0.3}Al_{0.1}$ annealed alloys.

Table 3
Hydrogen absorption/desorption characteristics for different annealed alloys.

Alloy (x)	Hydrogen content		Plateau pressure
	H/M	wt.%	Pa (atm)
$x = 0.1$	0.72	0.97	0.1
$x = 0.15$	1.06	1.43	0.1
$x = 0.2$	0.85	1.17	0.16
$x = 0.25$	1.00	1.40	0.39
$x = 0.3$	0.99	1.41	1.03
$x = 0.4$	0.72	1.08	7.32
$x = 0.5$	0.15	0.23	–

Pa is the pressure at midpoint of absorption hydrogen process.

Table 4
Summary of electrochemical performance for different annealed alloy electrodes at 293 K.

Alloys (x)	N	C_{max} (mAh g^{-1})	HRD_{900} (%)	S_{100} (%)	I_0 (mA g^{-1})	I_L (mA g^{-1})
$x = 0.1$	2	321.2	60.5	86.3	79.1	1610
$x = 0.15$	3	391.4	70.1	92.0	178.1	1580
$x = 0.2$	3	371.55	94.0	88.2	207.1	2030
$x = 0.25$	3	354.1	93.9	81.7	202.5	2100
$x = 0.3$	4	354.1	87.8	79.6	195.3	2030
$x = 0.4$	14	124.9	87.8	97.6	189.0	1130
$x = 0.5$	16	53.0	83.7	97.8	183.9	881

good activation properties except $x > 0.3$; four times of charge/discharge cycles were enough to activate electrodes. The maximal discharge capacity increased from 321.2 mAh g^{-1} ($x = 0.1$) to 391.4 mAh g^{-1} ($x = 0.15$) then decreased to 53 mAh g^{-1} with rise of Mg content, which may be due to the firstly increase of Ce_2Ni_7-type phase finally rise of $(La,Mg)(Ni,Co)_3$ and $La(Ni,Co)_5$ phase, $(La,Mg)(Ni,Co)_3$ alloy electrode exhibited poor cyclic stability [11].

Fig. 9 shows the cyclic stability curves of different annealed alloy electrodes. It can be found that cyclic stability was improved obviously from 86.3% ($x = 0.1$) to 92% ($x = 0.15$), which could be attributed to an amorphous effect in hydrogenation process and Ce_2Ni_7-type phase abundance in alloys [12]. Alloy electrode with $x = 0.15$ exhibits not only good cyclic stability ($S_{100} = 92\%$) but also high discharge capacity (391.4 mAh g^{-1}). The cyclic stability was deteriorated from 88.2% ($x = 0.2$) to 79.6% ($x = 0.3$) with the further increase of Mg content and the discharge capacity of the alloy electrode of $x > 0.3$ is very poor compared to other alloy electrodes, which could be attributed to the phase evolution in alloys. It should be noticed that the cycle stability was improved dramatically for $x = 0.15$. At the same time, the main phase was $(La,Mg)_2(Ni,Co)_7$ (Ce_2Ni_7-type) phase (93.4 wt.%). The experiment phenomenon indicates that cyclic stability of Ce_2Ni_7-type phase is much better than that of other phases. From Fig. 3, it can be concluded that decrease of $(LaMg)(Ni,Co)_3$ phase and $LaNi_5$ phase abundance and increase of Ce_2Ni_7-type phase abundance are important factors to improve cycle stability of annealing alloy electrodes. It is well known that degradation of discharge capacity for alloy electrodes can be influenced by two factors mainly: surface passivation of alloy electrodes because of oxidation of active composition and pulverization of alloy particles due to cell volume expansion in hydrogen absorption/desorption process [23]. In this paper, the single phase of Ce_2Ni_7-type and appropriate Mg content seem to be more important to influence cyclic stability of alloy electrodes since all alloys contained the same elements. Therefore, the poor cyclic stability of alloy electrode may be related to the following factors: (1) Fig. 7 shows an amorphous effect in hydrogenation process of $x = 0.1$, in which reversible ability of hydrogen absorption/desorption process was deteriorated. (2) The different corrosion rates of different phase structure. The study of F. Li [24] showed that the corrosion rates of these different phases are in order: $PuNi_3 \sim CeNi_3 > Ce_2Ni_7 > CaCu_5 \sim Ce_5Co_{19}$. Fig. 10 shows the Tafel polarization curves of different alloy electrodes at 293 K. The corrosion rates (v) can be attained according to the following equation [25]:

$$v = \left(3.6 \times 10^7\right) i_{corr} w/(nF) \quad (2)$$

where v and i_{corr} are proportional. So according to the corrosion current can be judged. Value of i_{corr} and E_{corr} is also listed in Table 5, it can be seen that the corrosion rates is in order: $x = 0.5 > x = 0.4 > x = 0.25$–$0.3 > x = 0.2 > x = 0.1$–$0.15$, and the corrosion potential order: $x = 0.15$–$0.25 > x = 0.3 > x = 0.1 > x = 0.4$–$0.5$, respectively. It can be concluded that the alloy for $x = 0.15$ have a property of corrosion resisting, which is consistent with that of the cyclic stability basically.

3.4. Electrochemical kinetic characteristics

Fig. 11 shows the high rate dischargeability (HRD) curves of different alloy electrodes. It can be found that Mg content increases

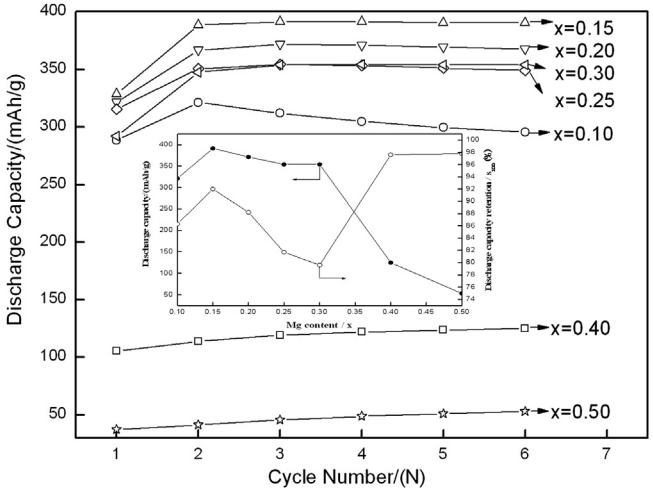

Fig. 8. Activation curves of $La_{0.8-x}Gd_{0.2}Mg_xNi_{3.1}Co_{0.3}Al_{0.1}$ ($x = 0.1$–0.5) annealed alloy electrodes with 60 mA g^{-1} charge–discharge current density at 293 K.

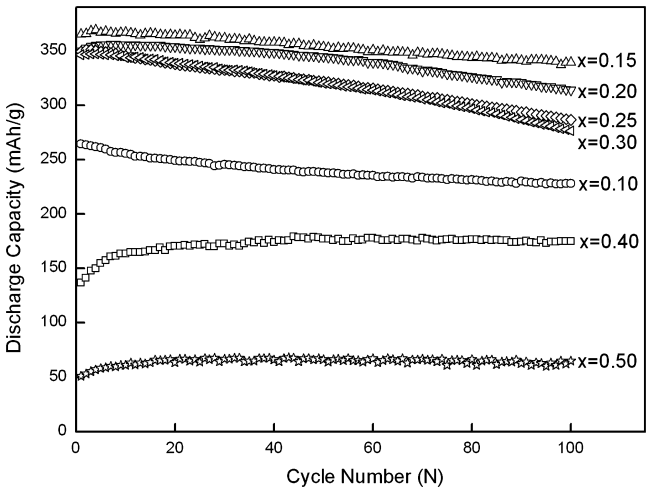

Fig. 9. Cyclic stability curves of $La_{0.8-x}Gd_{0.2}Mg_xNi_{3.1}Co_{0.3}Al_{0.1}$ ($x = 0.1$–0.5) annealed alloy electrodes with 300 mA g^{-1} charge–discharge current density at 293 K.

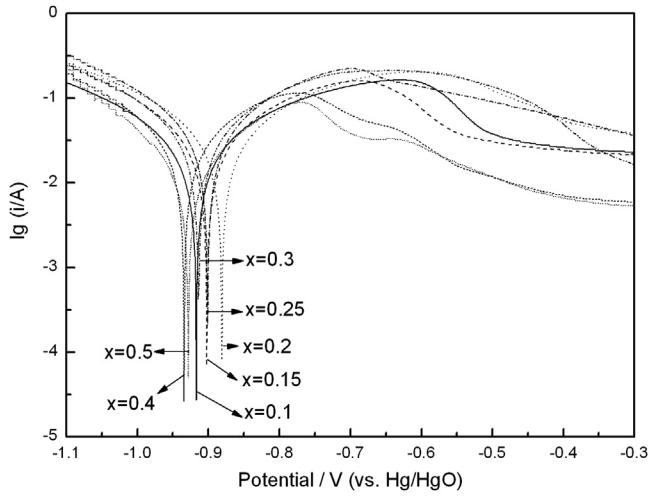

Fig. 10. Tafel polarization curves of $La_{0.8-x}Gd_{0.2}Mg_xNi_{3.1}Co_{0.3}Al_{0.1}$ alloy electrodes at 293 K.

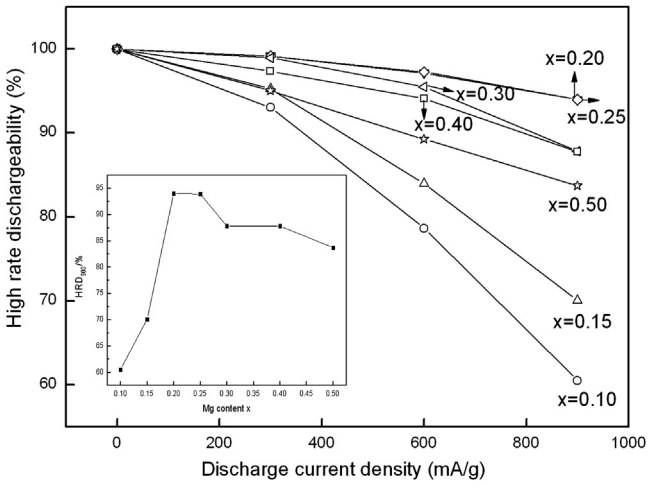

Fig. 11. High rate dischargeability (HRD) curves of $La_{0.8-x}Gd_{0.2}Mg_xNi_{3.1}Co_{0.3}Al_{0.1}$ ($x = 0.1$–0.5) annealed alloy electrodes at 293 K.

improved the HRD characteristic from 60.5% (HRD_{900}, $x = 0.1$) to 94% (HRD_{900}, $x = 0.2$). However, with the Mg content rise further, HRD_{900} decreased gradually from 93.9% ($x = 0.25$) to 83.7% ($x = 0.5$). However, it is excited that HRD_{900} for $x = 0.2$–0.25 increased to ~94% suddenly, which could be attributed to appearance of main phase $(La,Mg)_2(Ni,Co)_7$ and catalytic phase $La(Ni,Co)_5$ [26]. The experiment result shows that kinetic characteristic of $(La,Mg)_2(Ni,Co)_7$ phase is much better than that of $(La,Mg)(Ni,Co)_3$ phase.

The exchange current density I_0 is generally used to measure the kinetics of the electrochemical hydrogen reaction. Exchange current density (I_0) can be calculated according to the following equation [27]:

$$I_o = \frac{RTI_d}{F\eta} \tag{3}$$

where R is the gas constant, T is absolute temperature, I_d is the applied current density, F is the Faraday constant and η is the total overpotential. It is known that exchange current density (I_0) and limiting current density (I_L) are the other parameters to describe the kinetic characteristic of alloy electrodes. I_0 can be used to judge the speed of charge transfer on surface of alloy electrodes. I_L can be influenced by charge transfer, hydrogen diffusion and passivation of active composition. As shown in Table 4, I_0 increased from 73.1 mA g^{-1} ($x = 0.1$) to 207.1 mA g^{-1} ($x = 0.2$) then decreased to 783.9 mA g^{-1} ($x = 0.5$) and I_L increased from 1610 mA g^{-1} ($x = 0.1$) to 2100 mA g^{-1} ($x = 0.2$) then decreased to 881 mA g^{-1} ($x = 0.5$), respectively. It is clear that the reaction rate of hydrogen of alloy electrodes of $x = 0.2$, 0.25 is better than the other alloy electrodes. This change is in agreement with that of HRD.

The change of I_L verifies the influence of hydrogen diffusion on electrode reaction again. However, the change of I_L was not consistent with change of HRD. For example, the value of I_L alloy electrode of $x = 0.2$ is not the largest, but the HRD_{900} of alloy electrode of $x = 0.2$ is the best. This result implies with that hydrogen reaction rate in alloy bulk is more important to influence kinetic of electrode reaction. The decrease of I_0 of alloy electrode of $x > 0.25$ may be mainly due to the decrease of $(La,Mg)_2(Ni,Co)_7$ phase [11].

Table 5
Tafel fitting date of the $La_{0.8-x}Gd_{0.2}Mg_xNi_{3.1}Co_{0.3}Al_{0.1}$ alloys.

Alloy (x)	i_{corr}/(mA cm^{-2})	E_{corr}/V
$x = 0.1$	6.968	−0.9169
$x = 0.15$	6.968	−0.9019
$x = 0.2$	7.325	−0.8804
$x = 0.25$	8.777	−0.9004
$x = 0.3$	8.592	−0.9135
$x = 0.4$	10.451	−0.9340
$x = 0.5$	14.552	−0.9286

Calculated based on Tafel equation, i_{corr} is the corrosion current density, E_{corr} the corrosion potential.

4. Conclusion

The structure and electrochemical properties of different Mg content alloys have been studied systematically. Some conclusion can be summarized:

1) The main phase of $x = 0.1$–0.2 alloys is $(La,Mg)_2(Ni,Co)_7$ phase with Ce_2Ni_7-type structure. When Mg content increases from $x = 0.25$ to $x = 0.5$, some $(LaMg)(Ni,Co)_3$ phase with $PuNi_3$-type structure can appear. The lattice parameters of main phase represent a linear decrease with Mg content increase in alloys.
2) P–C isotherms show that the hydrogen storage capacity firstly increases from 0.97 wt.% to 1.43 wt.% and then decreases to 0.23 wt.% with rise of x. Meanwhile, hydrogen absorption plateau became firstly flatter and wider then higher and narrower with x increase. The studies of electrochemical characteristics show that alloy electrode of $La_{0.65}Gd_{0.2}Mg_{0.15}Ni_{3.1}Co_{0.3}Al_{0.1}$ exhibits the highest discharge capacity (391.4 mAh g^{-1}), good activation characteristic and better cyclic stability ($S_{100} = 92\%$).
3) With the increase of Mg content, the high rate dischargeability (HRD) at current density of 900 mA g^{-1} increases firstly from 60.5% ($x = 0.1$) to 94% ($x = 0.2$) and then decreases to 83.7% ($x = 0.5$). Alloys electrodes of $x = 0.2$, 0.25 exhibit good reaction rate of hydrogen and small charge-transfer resistance.

Acknowledgments

This work was supported by the National Nature Science Foundation of China (No. 50941019) and Ministry of Science and Technology of China (No. 2011AA03A408).

References

[1] T. Kohno, H. Yoshida, F. Kawashima, T. Inaba, I. Sakai, M. Yamamoto, et al., J. Alloys Compd. 311 (2000) L5–L7.
[2] T. Sakai, M. MatsuoKa, C. Iwakura, in: L. Eyring (Ed.), Handbook on the Physics and Chemistry of Rare Earths, Elesvier, Amsterdam, 1995, p. 133.
[3] F. Feng, M. Geng, D.O. Northwood, Int. J. Hydrogen Energy 26 (2001) 725–734.
[4] Gary Sandrock, J. Alloys Compd. 293–295 (1999) 877–888.
[5] J.J. Reilly, Metal Hydrides Electrode, in: J.O. Besenhard (Ed.), Handbook of Battery Materials, Wiley, New York, 2000.
[6] K. Kadir, T. Sakai, I. Uehara, J. Alloys Compd. 302 (2000) 112–117.
[7] K. Kadir, T. Sakai, I. Uehara, J. Alloys Compd. 257 (1997) 115–121.
[8] J.J. Reilly Jr., R.H. Wiswall Jr., Inorg. Chem. 7 (11) (1968) 2254–2256.
[9] Hongge Pan, Yongfeng Liu, Mingxia Gao, Yunfeng Zhu, Yongquan Lei, Int. J. Hydrogen Energy 28 (2003) 1219–1228.
[10] Hongge pan, Yongfeng Liu, Mingxia Gao, Yunfeng Zhu, Yongquan Lei, Qidong Wang, J. Alloys Compd. 351 (2003) 228–234.
[11] F.L. Zhang, Y.C. Luo, J.P. Chen, R.X. Yan, L. Kang, J.H. Chen, J. Power Sources 150 (2006) 247–254.
[12] F.L. Zhang, Y.C. Luo, R.X. Yan, L. Kang, J.H. Chen, J. Alloys Compd. 439 (2007) 181–188.
[13] S. Yasuoka, Y. Magari, T. Murata, T. Tanaka, J. Ishida, H. Nakamura, T. Nohma, M. Kihara, Y. Baba, H. Teraoka, J. Power Sources 156 (2) (2006) 662–666.
[14] R.V. Denys, B. Riabov, V.A. Yartys, R.G. Delaplane, M. Sato, J. Alloys Compd. 446-447 (2007) 166–172.
[15] R.V. Denys, B. Riabov, V.A. Yartys, R.G. Delaplane, M. Sato, J. Solid State Chem. 181 (2008) 812–821.
[16] R.V. Denys, V.A. Yartys, J. Alloys Compd. 509 (2011) S540–S548.
[17] Y.C. Luo, T. Wu, Z.J. Gao, R.F. Li, Z. Lin, L. Kang, J. Chin. Rare Earth Soc. 28 (3) (2010) 347–354.
[18] R.A. Young, in: R.A. Roung (Ed.), The Rietveld Method, IUCr. Oxford University Press, 1995.
[19] J. Rodriguez-Carvajal, in: Abstract of the Satellite Meeting on Powder Diffraction, Congress of IUCr, Toulouse, France (1990), p. 127. Fullprof Program, version 3.5d Oct 98-LLB-JRC, 1998.
[20] B. Liao, Y.Q. Lei, G.L. Lu, L.X. Chen, H.G. Pan, Q.D. Wang, J. Alloys Compd. 356–357 (2003) 746–749.
[21] K.H.J. Buschow, H.H. Van Mal, J. Less Common Met. 29 (1972) 203.
[22] J.J. Murray, M.L. Post, J.B. Taylor, J. Less Common Met. 80 (1981) 201–209.
[23] J.J.G. Willems, K.H.J. Buschow, J. Less Common Met. 129 (1987) 13.
[24] F. Li, K. Young, T. Ouchi, M.A. Fetcenko, J. Alloys Compd. 471 (2008) 371–377.
[25] K. Naito, N. Nastsunami, A.K. Shukla, J. Power Sources 63 (1996) 203–208.
[26] Yuan Li, Shumin Han, Jinhua Li, Lin Hu, Electrochim. Acta 52 (2007) 5945–5949.
[27] P.H.L. Notten, P. Hokkeling, J. Electrochem. Soc. 138 (1991) 1877–1885.